

Error propagation from the PIV-based pressure gradient to the integrated pressure by the omni-directional integration method

Xiaofeng Liu*, Jose Roberto Moreto

San Diego State University, Department of Aerospace Engineering, San Diego, California, USA

*Xiaofeng.Liu@sdsu.edu

Abstract

Characterization of the accuracy of the pressure reconstruction methods is of critical importance in understanding their capabilities and limitations. This paper reports for the first time a comprehensive theoretical analysis, numerical simulation and experimental validation of the error propagation characteristics for the omni-directional integration method, which has been used for pressure reconstruction from the PIV measured pressure gradient. The analysis shows that the omni-directional integration provides an effective mechanism in reducing the sensitivity of the reconstructed pressure to the random noise imbedded in the measured pressure gradient. Both the numerical and experimental validation results show that the omni-directional integration methods, especially the rotating parallel ray method, have better performance in data accuracy than the conventional Poisson equation approach in reconstructing pressure from noise embedded experimental data.

1 Introduction

Back in September, 2005, at the 6th ISPIV at Pasadena, California, the first author of this paper delivered an oral presentation with the title of “Instantaneous pressure and material acceleration measurements using a four exposure PIV system”, which introduced the principle of non-intrusive pressure measurement based on PIV and the novel omni-directional integration algorithm for pressure reconstruction from the measured pressure gradient, for which the measured material acceleration constitutes its dominant contributing term for high Reynolds number flow and in regions away from walls. Based on that presentation, a journal paper (Liu and Katz 2006) was published in *Experiments in Fluids*, marking the official introduction of the omni-directional integration pressure reconstruction method. The real advantage of the omni-directional integration method is its robust capability in accurate pressure reconstruction from the error-embedded experimental data, for which the conventional Poisson equation approach often encounters difficulty in defining the correct boundary conditions. The omni-directional integration method was further tested and applied to turbulent cavity flows (Liu and Katz 2008, 2013, 2018) and turbulent boundary layer flows (Joshi *et al.* 2014). Especially, the method recently evolved to an updated algorithm featuring rotating parallel ray (Liu *et al.* 2016) as integration path guidance, which brings improved accuracy in reconstructed pressure result. Subsequently, the new rotating parallel ray omni-directional integration algorithm was applied to 3D pressure reconstruction based on time-resolved tomographic PIV measurement of a turbulent channel flow over compliant wall (Zhang *et al.* 2017).

Characterization of the accuracy of the PIV pressure reconstruction methods is of critical importance in understanding the capabilities and limitations of these methods. Charonko *et al.* (2010), using a decaying Taylor vortex flow and two simulated pulsatile flow fields, demonstrated that the omni-directional method exhibits robust performance over the conventional Poisson equation approach for a wide range of resolutions, flow conditions and noise levels. Most recently, Wang *et al.* (2019) also demonstrated using DNS isotropic turbulence channel flows that the new rotating parallel ray omni-directional method has better performance than the conventional Poisson equation approach. As for theoretical analysis on error propagation, Pan *et al.* (2016) demonstrated in theory how the error propagates from the pressure gradient to the reconstructed pressure for the Poisson equation approach. However, up to date, there is no theoretical analysis available that characterizes the error propagation of the omni-directional integration method from the measured pressure gradient to the reconstructed pressure. To fill the gap, and help settle the question of why the omni-directional method has better performance over the conventional Poisson equation approach, this paper introduces a theoretical analysis for the error propagation characterization of the omni-directional integration method. The theoretical analysis is further validated by using both a direct numerical simulation database of isotropic turbulence flow and an experimental database for a turbulent shear layer flow.

2 The Omni-Directional Integration Method

2.1 Overview

Pressure can be obtained from PIV experiments in a two-step process: first the pressure gradient is computed from the velocity fields, then the second step is the integration of the pressure gradient to obtain the pressure field. The pressure gradient can be obtained using either the Eulerian approach (e.g. Gurka *et al.* 1999, Violato *et al.* 2011, de Kat and van Oudheusden 2012) where the unsteady and convection terms of the Eulerian expansion of the material acceleration are calculated directly as shown in equation (1), or the Lagrangian approach where the material acceleration is calculated directly by tracing imaginary fluid particles along their trajectories based on the so-called pseudo tracking method (e.g. Jensen *et al.* 2003, Liu and Katz 2006, Violato *et al.* 2011, de Kat and van Oudheusden 2012) as shown in equation (2). For high Reynolds number flows in regions away from walls, the viscous term is usually 3-4 orders of magnitude smaller than the pressure gradient term and therefore is negligible (Liu and Katz, 2006). In this case, the pressure gradient can be determined from the measured material acceleration.

$$\nabla p = -\rho \left[\frac{\partial \mathbf{u}}{\partial t} + (\mathbf{u} \cdot \nabla) \mathbf{u} - \nu \nabla^2 \mathbf{u} \right] \quad (1)$$

$$\nabla p = -\rho \left[\frac{D\mathbf{u}}{Dt} - \nu \nabla^2 \mathbf{u} \right] \quad (2)$$

The error propagation from velocity to acceleration was investigated by Jensen and Pedersen (2004), Violato *et al.* (2011), de Kat and van Oudheusden (2012), van Oudheusden (2013), Wang *et al.* (2016) and van Gent *et al.* (2017). Those investigations demonstrate that for advection dominated flows, the Lagrangian approach showed consistently less sensitivity to noise.

To reconstruct the pressure from the pressure gradient, one can use the Poisson equation for pressure as shown in equations (3) or (4), which are obtained by taking divergence of either Equation (1) or equation (2), respectively. An example of the implementation of the Poisson equation for pressure reconstruction can be found in de Kat and van Oudheusden (2012) and the error bounds for the Poisson solution can be found in Pan *et al.* (2016).

$$\nabla^2 p = -\rho \nabla \cdot \left[\frac{\partial \mathbf{u}}{\partial t} + (\mathbf{u} \cdot \nabla) \mathbf{u} - \nu \nabla^2 \mathbf{u} \right] \quad (3)$$

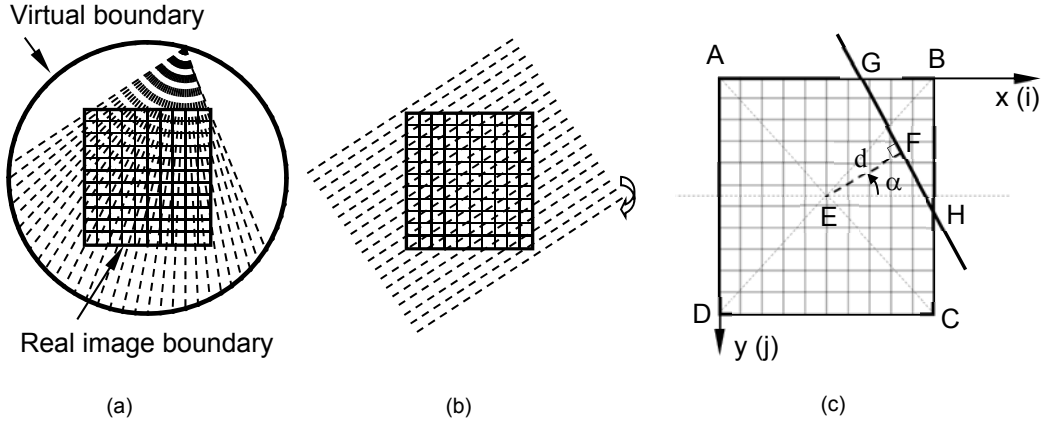


Figure 1. The omnidirectional algorithms. (a) The circular virtual boundary omni-directional integration algorithm. (b) The rotating parallel ray omni-directional integration algorithm. (c) Ray orientation with respect to the pressure calculation domain as a function of d (distance from the domain center) and α (ray rotation angle).

$$\nabla^2 p = -\rho \nabla \cdot \left[\frac{D\mathbf{u}}{Dt} - \nu \nabla^2 \mathbf{u} \right] \quad (4)$$

Equations (1) and (2) can be integrated directly by means of line integrals. While several approaches were proposed to perform the line integration (e.g., Baur and Kongeter 1999, Liu and Katz 2006, and Dabiri *et al.* 2014), the omnidirectional integration proposed by Liu and Katz (2006) showed the most robust results in the assessments of Charonko *et al.* (2010) and Wang *et al.* (2016).

In this paper, we present an analysis of the error propagation from the pressure gradient to the reconstructed pressure for the omni-directional integration methods (Liu and Katz 2003, 2006, 2008, 2013, and Liu *et al.* 2016) so as to elucidate the mechanisms for the random noise reduction that grants the robustness of the method. To facilitate the analysis, details about the history and principle of the omni-directional integration method are described below.

2.2 The Omni-directional Integration

The omni-directional integration of the pressure gradient for obtaining pressure from PIV experiments was proposed by Liu and Katz (2003), which integrates the measured pressure gradient by following the shortest integration paths across the integration domain connecting the domain boundary points. To determine the pressure at an internal nodal point in the field of view, the local pressure values obtained from the integration paths passing by the internal nodal point are averaged so as to minimize the influence of the error embedded in the pressure gradient measurement. This method was later improved by placing a virtual boundary outside the real flow field domain and allowing the integration paths originate from and end at the virtual boundary (Liu and Katz 2006) so as to reduce the path clustering close to the real boundaries. A further development was introduced by Liu and Katz (2008, 2013) by using a circular virtual boundary. The most recent improvement in the omnidirectional integration methods was introduced by Liu *et al.* (2016), using rotating parallel rays as integration guide lines.

The essence of the Omni-Directional Integration is to minimize the influence of the errors embedded in the measured acceleration data on the final pressure result, to achieve a reliable and accurate pressure measurement. The pressure integration arrangement is based on the fact that the pressure is a scalar potential, therefore the spatial integration of the pressure gradient must be independent of the integration path. As shown in Fig. 1(a), the discrete points distributed uniformly along the circular virtual boundary serve as guiding points to define the orientation and position of the integration paths. A group of “virtual” integration paths start from one point and end at other points on the virtual boundary, creating a ray pattern of integration paths that cover the real field of view. The actual integration starts from and stops at the real boundaries, in a “zig-zag” fashion,

along real nodal points that have the shortest distance to the integration paths. Each time the integration path crosses a certain internal node, the result of integration is stored in a data bin associated with that internal node. This procedure is repeated for all the virtual boundary nodes. Averaging all the values stored in data bins provides the result of the omni-directional integration.

One shortcoming of the Circular Virtual Boundary omnidirectional integration method is that except the points near the geometric center of the real integration domain, points at other places do not see an axisymmetric distribution of the integration paths, which results in a non-uniform weight contribution to the final integration. To overcome this inherent defect, Liu *et al.* (2016) introduces a new algorithm featuring rotating parallel ray (Fig. 1b) as integration path guidance. Unlike the virtual boundary omni-directional method, the new Rotating Parallel Ray Omni-Directional Integration method utilizes parallel rays as guidance for integration paths. The parallel rays can be viewed as being originated from a virtual boundary at an infinity distance from the real boundary. Effectively, by rotating the parallel rays, omni-directional paths with equal weights coming from all directions toward the point of interest at any location within the computation domain will be generated. In this way, the location dependence of the integration weight due to an inherent defect (though not significant) in virtual path arrangement in the old algorithm will be eliminated.

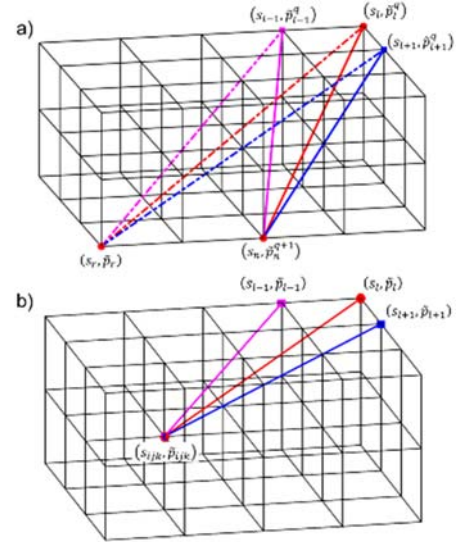


Figure 2. (a) Integration path connections among boundary points for omni-directional integration; (b) Integration path connection between inner nodal point and boundary points.

For all the omnidirectional integration methods the following procedures must be applied adequately to reduce error propagation from the boundaries:

- 1) Boundary pressure calculation.
 - a) Set a pressure reference point.
 - b) Initialize pressure values on the boundary points.
 - c) Integrate the pressure gradient field using the specific method of the omni integration.
 - d) Update the boundary pressure values with the newly calculated data.
 - e) Iterate until prescribed accuracy is achieved.
- 2) Inner domain pressure calculation.

3 Error Propagation Analysis

We can show that for the omni-directional integration methods, the pressure error $\epsilon_n^{(q+1)}$ at a boundary point s_n (Figure 2) after each q round of iteration contains three terms, as shown below.

$$\epsilon_n^{(q+1)} = \epsilon_{nB}^q + \epsilon_{nA} + \epsilon_{ref} \quad (5)$$

where ϵ_{ref} denotes the error embedded in the reference pressure point,

$$\epsilon_{nA} = \sum_{l=1}^M \left[\frac{R(l, n)}{N_n} \left(\epsilon_{t(l, n)} + \int_{s_l}^{s_n} \epsilon_{\nabla p} \cdot \mathbf{ds} \right) - \frac{R(l, r)}{N_r} \left(\epsilon_{t(l, r)} + \int_{s_l}^{s_r} \epsilon_{\nabla p} \cdot \mathbf{ds} \right) \right] \quad (6)$$

and

$$\epsilon_{nB}^q = \sum_{l=1}^M \left\{ \left(\frac{R(l, n)}{N_n} - \frac{R(l, r)}{N_r} \right) \epsilon_l^q \right\} \equiv \sum_{l=1}^M (w(l, n) \cdot \epsilon_l^q) \quad (7)$$

where the weight $w(l, n)$ that is applied to the boundary pressure value is defined as

$$w(l, n) = \frac{R(l, n)}{N_n} - \frac{R(l, r)}{N_r} \quad (8)$$

In the above equations, $R(l, n)$ represents the number of repetitive integration path connections ($R(l, n) \geq 1$) between boundary points s_l and s_n ; $N_n = \sum_{l=1}^M R(l, n)$; $N_r = \sum_{l=1}^M R(l, r)$, with M being the total number of the boundary points over the entire computation domain, r corresponding to reference boundary point s_r ; $\epsilon_{t(l, n)}$ the numerical truncation error for the pressure integration along the path connecting boundary points s_l and s_n ; $\epsilon_{t(l, r)}$ the numerical truncation error for the pressure integration along the path connecting boundary points s_l and s_r ; and $\epsilon_{\nabla p}$ the error embedded in the measured pressure gradient field. Consequently, according to equation (6), ϵ_{nA} is a fixed value which is independent of the number of iterations at the given boundary point location s_n .

For a given measurement domain, the weight $w(l, n)$ depends only on the omnidirectional integration method used in the pressure reconstruction. It does not depend on the noise level in the measured pressure gradient field. For the rotating parallel ray method, the weight $w(l, n)$ depends on the ray density, i.e, the parameter of $(\Delta\alpha, \Delta d)$, as defined in Fig. 1(c). Increasing the ray density decreases the weight magnitude. For a dense enough ray configuration used in this study ($\Delta\alpha = 0.20, \Delta d = 0.4$), the weight magnitude is on the order of $O(10^{-3})$.

It can be shown that the implicit recursive relation for the pressure error at the domain boundary as shown in equation (5) can be written as:

$$\epsilon_n^q = \lambda_{n, max}^q C_{n, max} + \epsilon_{nA} + \epsilon_{ref} \quad (9)$$

where $C_{n, max}$ is a constant that depends on the pressure initialization at the boundary points ($q = 0$) and $\lambda_{n, max}$ is the characteristic error decay rate that depends on the omnidirectional integration algorithm used. For the rotating parallel ray omnidirectional integration with an adequate ray density, $|\lambda_{n, max}| < 1$. After sufficient amount of iterations, the final error converges to:

$$\epsilon_n^{qend} \approx \epsilon_{nA} + \epsilon_{ref} \quad (10)$$

which implies that, according to equation (5), $\epsilon_{nB}^{qend} \approx 0$. The characteristic error decay rate $|\lambda_{n, max}|$ can be obtained from the following relationship, with $P_{n, max}(q)$ being a constant:

$$\log_{10} |\epsilon_n^q - \epsilon_n^{qend}| = q \log_{10} |\lambda_{n, max}| + \log_{10} |P_{n, max}(q)| \quad (11)$$

For the pressure error ϵ_{ijk} at an inner nodal point (Fig. 2b), it can be shown that

$$\epsilon_{ijk} = \frac{1}{N_{ijk}} \sum_{l=1}^M \left[R(l, ijk) \left(\epsilon_l + \epsilon_{t(l, ijk)} + \int_{s_l}^{s_{ijk}} \epsilon_{\nabla p} \cdot ds \right) \right] \quad (12)$$

Equation (12) shows that the pressure error at an inner nodal point is the average over all the number of integration paths N_{ijk} for the combination of the pressure error (ϵ_l) at boundary point s_l , the truncation error ($\epsilon_{t(l, ijk)}$) along the path from boundary point s_l to inner nodal point s_{ijk} , and the line integration of the error embedded in the pressure gradient $\epsilon_{\nabla p}$ along the path from s_l to s_{ijk} . Assuming the error embedded in the pressure gradient is random and homogeneously distributed in space, the third term in equation (12) will vanish after the spatial averaging over all the integration paths involved in the calculation. Consequently, in that case, the error at an inner nodal point can be simplified as:

$$\epsilon_{ijk} \approx \frac{1}{N_{ijk}} \sum_{l=1}^M \left[R(l, ijk) \left(\epsilon_l + \epsilon_{t(l, ijk)} \right) \right] \quad (13)$$

4 Results

To validate the error propagation model for omnidirectional integration, we utilize direct numerical simulation (DNS) data of homogeneous isotropic turbulence flow available to the public from the John Hopkins University Turbulence Database (JHTDB, see details about the database in Perlman *et al.* 2007 and Li *et al.* 2008). From the database, we select a sample plane containing 256×256 grid nodal points. At each of these nodal points, the exact pressure value and the pressure gradient components $\frac{dp}{dx}$ and $\frac{dp}{dy}$ obtained using central finite difference are available. To simulate the measurement uncertainties, 1000 statistically independent random noise with standard uniform spatial distributions and zero mean value are embedded in the pressure gradient, creating 1000 sample realizations of pressure gradient distribution for the pressure reconstruction error investigation. The random noise is generated using a built-in Matlab® function “rand”, with 1000 distinct seed numbers. The noise amplitude is set as 40% of the maximum magnitude of the pressure gradient in the sample DNS planar data.

As shown in equations (5) and (7), the convergence of the boundary pressure error $\epsilon_n^{(q+1)}$ is achieved through the error term ϵ_{nB}^q , which in turn relies on the weight coefficient matrix $w(l, n)$ that applies to the boundary pressure error ϵ_l^q to reduce the error. As discussed in Section 3, $|w(l, n)| \ll 1$ for a sufficiently dense parallel ray configuration, which provides the basis for $\epsilon_{nB}^{q\text{end}} \approx 0$ and ϵ_l^q eventually reduced to $\epsilon_n^{q\text{end}} \approx \epsilon_{nA} + \epsilon_{ref}$ (i.e., equation 10). To show this evolution process, Figure 3 presents the boundary pressure error convergence process for pressure error ϵ_n^q and error components ϵ_{nA} and ϵ_{nB}^q with respect to iteration round q at all boundary points for representative isotropic turbulence test cases with and without added noise. As mentioned in Section 3, ϵ_{nA} does not change through iteration. This observation is verified in Fig. 3 by examining the evolution process of ϵ_{nA} for both test cases (i.e., with and without added noise). In contrast, the overall amplitudes for both ϵ_n^q and ϵ_{nB}^q decay gradually through iteration, with their final values converged to $\epsilon_n^{q\text{end}} \approx \epsilon_{nA} + \epsilon_{ref} = \epsilon_{nA}$ (where $\epsilon_{ref} = 0$ for both cases) and $\epsilon_{nB}^{q\text{end}} \approx 0$, respectively, as expected.

The characteristic error decay rate $|\lambda_{n,max}|$ for pressure error at each boundary point can be obtained from equation (11). To facilitate a conservative evaluation, the maximum absolute values of the characteristic error decay rate of the boundary pressure error for all boundary points at

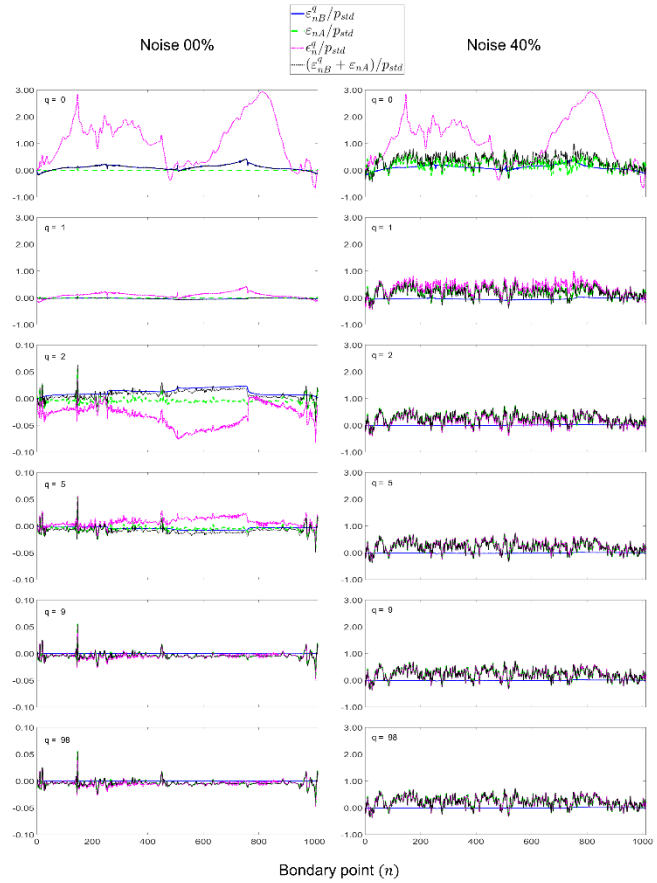


Figure 3. The evolution of the boundary pressure error convergence for the pressure error ϵ_n^q and the error components ϵ_{nA}^q , and ϵ_{nB}^q at representative iteration rounds. The left column shows the error evolution for the isotropic turbulence test case without noise added. The right column shows the error evolution for the test case with 40% noise added to the pressure gradient field. For both cases, $\epsilon_{ref} = 0$. Please note the y-axis scales for $q=1$ and 2 on the left column are different from the rest plots in that column. Also please note, the initial error distributions ϵ_n^1 for both testing cases are the same because of the zero boundary value initialization for both cases.

different parallel ray configuration and noise conditions (e.g., with and without added noise) are listed in Table 1. From Table 1 it can be seen that $(|\lambda_{n,max}|)_{max} < 1$ for all cases tested as expected, indicating $|\lambda_{n,max}| < 1$ for all boundary pressure errors for these cases. The high values of the minimum coefficient of determination $(R^2)_{min}$ indicate the logarithmic relationship shown in equation (11) has a high degree of correlation if the density of the integration paths are adequately high.

Table 1. The maximum value of the characteristic error decay rate of boundary pressure error for all boundary points.

Percentage noise added	Parallel Ray configuration parameters	The maximum characteristic error decay rate $(\lambda_{n,max})_{max}$	The minimum coefficient of determination $(R^2)_{min}$
0.0%	$(\Delta\alpha = 0.04^\circ, \Delta d = 0.4)$	0.36	0.9997
0.0%	$(\Delta\alpha = 0.20^\circ, \Delta d = 0.4)$	0.41	0.9991
0.0%	$(\Delta\alpha = 3.00^\circ, \Delta d = 0.4)$	0.57	0.8252
40.0%	$(\Delta\alpha = 0.04^\circ, \Delta d = 0.4)$	0.38	0.9981
40.0%	$(\Delta\alpha = 0.20^\circ, \Delta d = 0.4)$	0.39	0.9999
40.0%	$(\Delta\alpha = 3.00^\circ, \Delta d = 0.4)$	0.57	0.8682

Following equation (11), the decay of the averaged boundary pressure error is examined in Figure 4. It can be seen from Figure 4 that both the dense integration lines (Fig. 4a_i and b_i) and the high grid spatial resolution (Fig. 4a_ii and b_ii) help expedite the overall rate of convergence. The imbedded noise level also has an effect of reducing the error decay rate by comparing Fig. 4(a) and (b).

Figure 5 presents the cumulative average of the standard deviation error ϵ_{std} and the maximum and minimum error bounds found for the pressure reconstructed using the aforementioned integration methods. In Fig. 5, all quantities are normalized by the standard deviation of the DNS pressure p_{std} obtained in the original 256×256 sample planar domain. From Fig. 5(a), it can be seen that there exists a significant difference between the error bounds for the omnidirectional integration methods and that of the Poisson method with Neumann boundary condition (Poisson NBC). For the omnidirectional methods, the errors are always below 0.25 while the upper error bound for the Poisson NBC exceeds 2.67, i.e., about one order of magnitude higher. Also, the average errors for the omnidirectional integration methods are below 0.17 and the average error for Poisson NBC is about 0.86. To further discern the performance difference between the two omnidirectional integration methods investigated, a zoomed-in version of Fig. 5(a) is shown in Fig. 5(b), from which the improvement in performance

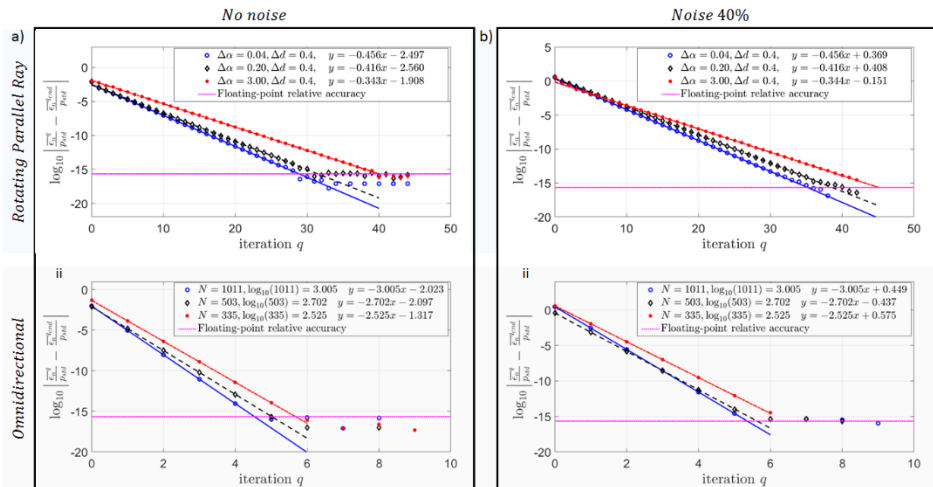


Figure 4. Boundary pressure error convergence for the pressure reconstructed from a pressure gradient field (a) without added noise and (b) with the 40% embedded noise. Please note in (a-ii) and (b-ii), The three grids have the same domain size but different cell size. $N = 1011$ corresponds to a grid of (254×254) , i.e., the original grid; $N = 503$ corresponds to a grid of (127×127) , achieved by sampling every other point over the original grid; and $N = 335$ corresponds to (85×85) , achieved by skipping two points for sampling.

from the circular virtual boundary omnidirectional integration method to the rotating parallel ray omnidirectional integration method can be clearly seen. It is important to note that, as shown in Liu *et al.* (2016), the performance of the rotating parallel ray depends on the incremental rotation angle $\Delta\alpha$ and the distance between rays Δd (normalized by the grid spacing). For the isotropic turbulence DNS data investigated in this work, the optimal pressure reconstruction result is obtained when $\Delta d = 0.4$ and $\Delta\alpha = 0.2^\circ$ for the rotating parallel ray pressure reconstruction method.

Figure 5(b) also highlights the benefit of using the rotating parallel ray omnidirectional integration to generate Dirichlet boundary conditions that are then applied to the Poisson equation for pressure (Poisson DBC_{Parallel Ray}). It can be seen from Fig. 5(b) that using the Dirichlet boundary conditions achieved by the optimal parallel ray omnidirectional integration, the Poisson DBC method performs better than the virtual boundary omnidirectional integration method, while it is still slightly outperformed by the optimal parallel ray omnidirectional integration method by 0.2% with respect to p_{std} . Table 2 summarizes the average error, the standard deviation of the error and the maximum error for the 1000 pressure field realizations reconstructed from the corresponding pressure gradient field of a DNS of isotropic turbulence with the 40% embedded random noise. As can be seen from Table 2, the mean error for the Poisson NBC approach is one order of magnitude higher than the omnidirectional methods.

To verify the performance of the pressure reconstruction methods in processing experimental data, the methods tested above are also applied to pressure reconstruction from a measured pressure gradient field database for a turbulent shear layer flow over an open cavity (Liu and Katz 2013 and 2018). The results are compared in terms of mean and rms pressure distributions (Fig.6) as well as probability density function profiles of pressure fluctuation at selected locations in the shear layer (Fig. 7). The experiment regarding the turbulent cavity shear layer flow has been described in detail in Liu and Katz (2013 and 2018). A turbulent boundary layer with a shape factor of 1.70 separates from the leading edge of a 2-D open cavity, forming a turbulent shear layer over the cavity. Time-resolved planar PIV data, sampled at 4500 frames per second, have been obtained at a Reynolds number of 4.0×10^4 based on the cavity length of 38.1mm and the free stream speed of $U_\infty = 1.20$ m/s. The pressure gradient field has been obtained based on the Lagrangian acceleration measurement, as discussed in Section 1. A sample of 9,994 sequentially obtained instantaneous realizations of pressure gradient field with a field of view of 25×25 mm located immediately upstream of the cavity trailing edge are utilized in the current study to compare the pressure reconstruction performance.

From Fig. 6, it can be seen that, similar to the performance comparison results based on the error-embedded DNS isotropic turbulence, for the experimental data, except the Poisson equation NBC approach, the performance for the other three pressure reconstruction methods evaluated, i.e., the

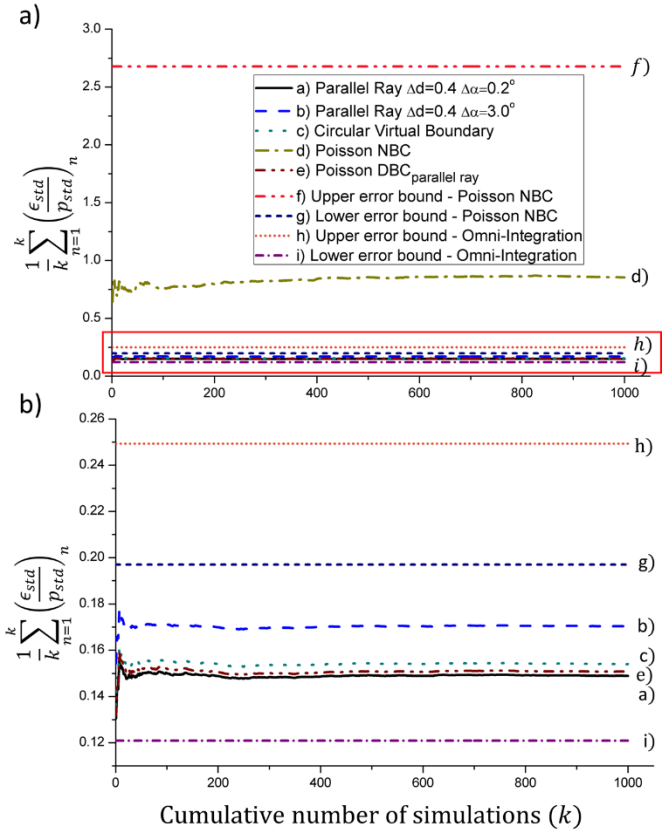


Figure 5. (a) Cumulatively averaged standard deviation of the pressure error for the 1000 reconstructed pressure realizations of the isotropic turbulence flow with 40% random noise embedded in the pressure gradient field. (b) Zoomed-in plot showing the details of the comparison among the methods tested.

Circular Virtual Boundary Omnidirectional Integration, the Rotational Parallel Ray Omnidirectional Integration ($\Delta\alpha = 0.2^\circ, \Delta d = 0.4$), and the Poisson equation method with the parallel ray generated Dirichlet boundary condition, can all capture the essential features of the mean and rms pressure distributions if compared with the corresponding results in Liu and Katz (2013). In contrast, the Poisson equation with Neumann boundary condition fails to capture the pressure field correctly.

Table 2: Average error and the error standard deviation of the 1000 statistically independent reconstructed pressure realizations based on a sample pressure gradient field from the JHU isotropic turbulence database embedded with random noise at an amplitude of 40% of the maximum pressure gradient.

Method	$\frac{1}{1000} \sum_{n=1}^{1000} \left(\frac{\epsilon_{std}}{p_{std}} \right)_n$	$\left(\frac{\epsilon_{std}}{p_{std}} \right)_{std}$	$\left(\frac{\epsilon_{std}}{p_{std}} \right)_{max}$
Rotating Parallel Ray $\Delta r = 0.4, \Delta\alpha = 0.2$	0.149	0.015	0.231
Rotating Parallel Ray $\Delta r = 0.4, \Delta\alpha = 3.0$	0.170	0.014	0.249
Circular Virtual Boundary Integration	0.154	0.015	0.232
Poisson Solution with Parallel Ray results as Dirichlet Boundary Condition	0.151	0.015	0.230
Poisson Solution Neumann Boundary Condition	0.854	0.406	2.678

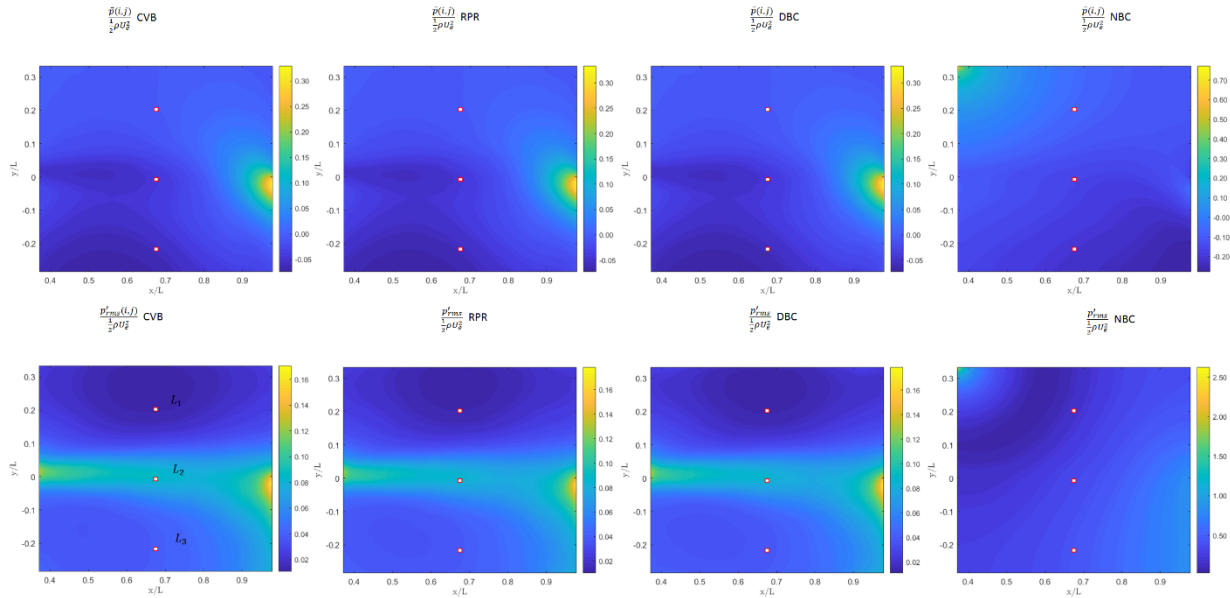


Figure 6. Mean and rms pressure distributions obtained using the Circular Virtual Boundary Omnidirectional Integration (abbreviated as CVB), the Rotational Parallel Ray Omnidirectional Integration with $\Delta\alpha = 0.2^\circ$ and $\Delta d = 0.4$ (RPR), the Poisson Equation method with the parallel ray generated Dirichlet Boundary Condition (DBC) and the Poisson Equation method with Neumann Boundary Condition (NBC) pressure reconstruction methods. for a turbulent shear layer flow over a 2D open cavity at Reynolds number of 4×10^4 .

To further verify the above results, Figure 7 shows the comparison of the probability density function profiles for the fluctuation pressure obtained by these four pressure reconstruction methods at representative sample locations L_1 (in the free stream region), L_2 (in the shear layer) and L_3 (in the cavity recirculation region) as indicated in Fig. 6. It can be seen that, except the result obtained by the Poisson equation with Neumann boundary condition, the fluctuation pressure range predicted by the other three methods agree with each other. The mismatch at the tails of the profiles shown in Fig. 6(d), (e) and (f) is presumably due to lack of convergence because of the rare flow events corresponding to those fluctuation range. In contrast, the Poisson equation with Neumann

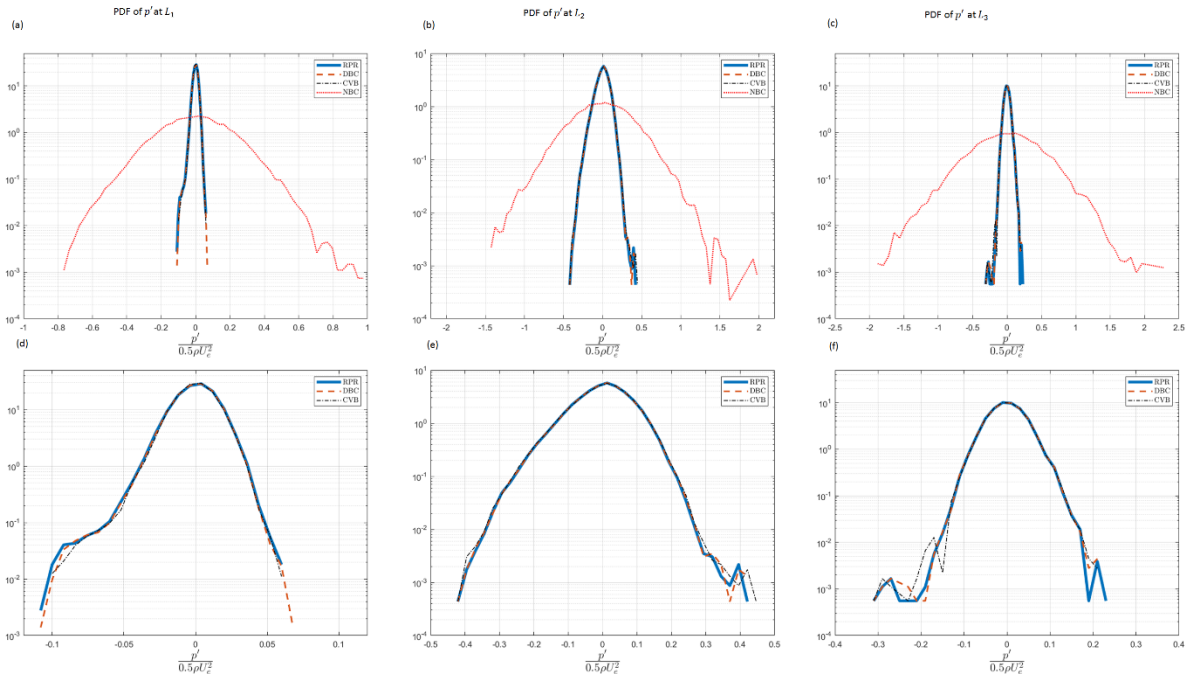


Figure 7. Comparison of the probability density function profiles for the fluctuation pressure at sample locations L_1 , L_2 and L_3 indicated in Fig. 6 for a turbulent shear layer flow over a 2D open cavity at Reynolds number of 4.0×10^4 . The PDF profiles in the lower row are zoomed-in plots for the corresponding upper row plots.

boundary condition once again brings a significantly over-predicted pressure fluctuation range, which is unrealistic.

5 Conclusion

This paper reports for the first time a theoretical analysis and the corresponding numerical and experimental validation of the error propagation characteristics for the omni-directional integration method, which has been used for pressure reconstruction from the PIV measured pressure gradient. The analysis shows that the omni-directional integration provides an effective mechanism in reducing the sensitivity of the reconstructed pressure to the random noise imbedded in the measured pressure gradient. Accurate determination of the boundary pressure values is the first step in ensuring the accuracy of the final reconstructed pressure. The boundary pressure error consists of two parts, with one part decaying in magnitude and eventually vanishing, and the other remaining as a constant with small magnitude through an iteration process.

These results are verified by using a direct numerical simulation database of isotropic turbulence flow with homogeneously distributed random noise added to the entire field of the pressure gradient to simulate noise embedded data. For the 1000 statistically independent pressure gradient field realizations with a 40% added noise, the nondimensionalized average error of the reconstructed pressure is 0.854 ± 0.406 for the pressure Poisson equation with Neumann boundary condition, 0.154 ± 0.015 for the circular virtual boundary omni-directional integration and 0.149 ± 0.015 for the rotating parallel ray omni-directional integration. If the converged boundary pressure values obtained by the rotating parallel ray method are used as the Dirichlet boundary conditions, the nondimensionalized average error of the reconstructed pressure by Poisson is reduced to 0.151 ± 0.015 . Of the different variations of the omni-directional methods, the parallel ray method shows the best performance and therefore is the method of choice.

Comparisons of these pressure reconstruction methods using an experimentally obtained turbulent shear layer flow over an open cavity are in agreement with the conclusions obtained with the DNS

turbulence data. Both the numerical and experimental validation results demonstrate that the omnidirectional integration methods, especially the rotating parallel ray method, have better performance in data accuracy than the conventional Poisson equation approach in reconstructing pressure from noise embedded experimental data.

Since there are numerous occasions in science and engineering practice that require the solution of a scalar potential from a conservative vector field using Poisson equation, e.g., the reconstruction of temperature or wavefront distributions from their corresponding gradients, the omnidirectional integration methods, especially the parallel ray omnidirectional integration method, are readily applicable to those generic occasions in scalar reconstruction from their error contaminated gradient data.

Acknowledgements

This work has been sponsored in part by the Office of Naval Research grant N00014-19-1-2020 (K.-H. Kim is the Program Officer), the National Science Foundation grant 1933176 (R. Joslin is the Program Director) and the San Diego State University UGP program 2015. The authors would like to thank Prof. J. Katz for his permission of the use of the Hopkins cavity research data in this study. J.R. Moreto, a doctoral student in the San Diego State University-University of California, San Diego Joint Doctoral Program, acknowledges the support of the 2018/19 University Graduate Fellowship from the San Diego State University. Both authors contributed equally to this paper.

References

- Baur T and Kongeter J (1999) PIV with high temporal resolution for the determination of local pressure reductions from turbulent phenomena. *Workshop on particle image velocimetry* (Santa Barbara, CA) pp 101–6
- Charonko JJ, King CV, Smith BL and Vlachos PP (2010) Assessment of pressure field calculations from particle image velocimetry measurements. *Meas. Sci. Technol.* 21(10):105401
- Dabiri JO, Bose S, Gemmell BJ, Colin SP and Costello JH (2014) An algorithm to estimate unsteady and quasi-steady pressure fields from velocity field measurements. *J. Exp. Biol.* 217:331–6
- van Gent PL, Michaelis D, van Oudheusden BW, Weiss PÉ, de Kat R, Laskari A, Jeon Y J, David L, Schanz D, Huhn F, Gesemann S, Novara M, McPhaden C, Neeteson NJ, Rival DE, Schneiders JFG and Schrijer FFJ (2017) Comparative assessment of pressure field reconstructions from particle image velocimetry measurements and Lagrangian particle tracking. *Exp. Fluids* 58:33
- Gurka R, Liberzon A, Hefetz D, Rubinstein D and Shavit U (1999) Computation of pressure distribution using PIV velocity data. *Workshop on particle image velocimetry* vol 2 (Santa Barbara, CA) pp 1–6
- Jensen A and Pedersen GK (2004) Optimization of acceleration measurements using PIV. *Meas. Sci. Technol.* 15:2275–83
- Jensen A, Pedersen GK and Wood DJ (2003) An experimental study of wave run-up at a steep beach. *J. Fluid Mech.* 486:161–88
- Joshi P, Liu X and Katz J (2014) Effect of mean and fluctuating pressure gradients on boundary layer turbulence. *J. Fluid Mech.* 748:36–84

- de Kat R and van Oudheusden BW (2012) Instantaneous planar pressure determination from PIV in turbulent flow. *Exp. Fluids* 52:1089–106
- Li Y, Perlman E, Wan M, Yang Y, Meneveau C, Burns R, Chen S, Szalay A and Eyink G (2008) A public turbulence database cluster and applications to study Lagrangian evolution of velocity increments in turbulence. *J. Turbul.* 9:N31
- Liu X and Katz J (2003) Measurements of pressure distribution by integrating the material acceleration Fifth International Symposium on Cavitation (Osaka, Japan)
- Liu X and Katz J (2006) Instantaneous pressure and material acceleration measurements using a four-exposure PIV system *Experiments in Fluids* 41:227–40
- Liu X and Katz J (2008) Cavitation phenomena occurring due to interaction of shear layer vortices with the trailing corner of a two-dimensional open cavity. *Phys. Fluids* 20(4), 041702
- Liu X and Katz J (2013) Vortex-corner interactions in a cavity shear layer elucidated by time-resolved measurements of the pressure field. *J. Fluid Mech.* 728:417–57
- Liu X and Katz J (2018) Pressure–Rate-of-Strain, Pressure Diffusion, and Velocity–Pressure-Gradient Tensor Measurements in a Cavity Flow. *AIAA J.* 56:3897–914
- Liu X, Moreto JR and Siddle-Mitchell S (2016) Instantaneous Pressure Reconstruction from Measured Pressure Gradient using Rotating Parallel Ray Method, *AIAA-2016-1049, 54th AIAA Aerospace Sciences Meeting, AIAA SciTech*, doi: 10.2514/6.2016-1049.
- van Oudheusden BW (2013) PIV-based pressure measurement. *Meas. Sci. Technol.* 24:032001
- Pan Z, Whitehead J, Thomson S and Truscott T (2016) Error propagation dynamics of PIV-based pressure field calculations: How well does the pressure Poisson solver perform inherently? *Meas. Sci. Technol.* 27(8), 084012.
- Perlman E, Burns R, Li Y and Meneveau C (2007) Data exploration of turbulence simulations using a database cluster *Proceedings of the 2007 ACM/IEEE conference on Supercomputing - SC '07* (New York, New York, USA: ACM Press)
- Violato D, Moore P and Scarano F (2011) Lagrangian and Eulerian pressure field evaluation of rod-airfoil flow from time-resolved tomographic PIV. *Exp. Fluids* 50(4): 1057–70
- Wang Z, Gao Q, Wang C, Wei R and Wang J (2016) An irrotation correction on pressure gradient and orthogonal-path integration for PIV-based pressure reconstruction. *Exp. Fluids* 57:104
- Wang J, Zhang C, and Katz J (2019) GPU-based, parallel-line, omni-directional integration of measured pressure gradient field to obtain the 3D pressure distribution. *Experiments in Fluids*, 60(4), 58.
- Zhang C, Wang J, Blake W and Katz J (2017) Deformation of a compliant wall in a turbulent channel flow. *J. Fluid Mech.* 823:345–90